Article

Large riverbed sediment flux sustained for a decade after an earthquake

https://doi.org/10.1038/s41586-025-09354-8

Received: 7 December 2024

Accepted: 2 July 2025

Published online: 13 August 2025

Check for updates

Gen K. Li[1,2,3]✉, A. Joshua West[2], Zhangdong Jin[4,5,6], Hongrui Qiu[7], Fei Zhang[4,8], Jin Wang[4,6], Douglas E. Hammond[2], Alexander L. Densmore[9], Robert G. Hilton[10], Sijia Dong[2,3,11], Abra Atwood[2,12], Woodward W. Fischer[3] & Michael P. Lamb[3]

Large earthquakes induce widespread landslides that fill river channels with sediment[1,2], generating long-lasting fluvial hazards and reshaping mountain topography. However, riverine sediment fluxes after earthquakes remain poorly resolved, mostly because of a lack of data on bedload flux[3,4]. Here we construct a source-to-sink sediment budget following the 2008 M_w7.9 (where M_w is the moment magnitude) Wenchuan earthquake in the eastern Tibetan mountains. We measured sediment accumulation in a man-made reservoir downstream of the earthquake-affected region. Ten years after the earthquake, the Min Jiang River had exported about 9% of the sediment mass from earthquake-triggered landslides, with around 5.7 times increase in the total riverine sediment flux sustained over that time. Bedload flux increased by $27.4^{+14.6}_{-15.6}$% times compared with pre-earthquake levels, making up 65^{+12}_{-26}% of the post-earthquake sediment export—a proportion much higher than typical of most mountainous rivers. At the current pace, the river system will remove most Wenchuan landslide debris over centennial timescales. However, future sediment export rates are likely to vary because of changes on hillslopes (for example, revegetation) and in hydrology, sediment characteristics and transport processes. Our findings demonstrate a decadal bedload-dominated sediment pulse driven by earthquake-triggered landslides, suggesting that increased vulnerability to cascading hazards such as aggradation and flooding could persist for decades in populated downstream regions after a large earthquake.

In tectonically active mountain ranges, strong shaking during earthquakes can induce widespread landslides[1,2]. These landslides erode soil and bedrock from hillslopes, and this material can then be entrained and transported by mountainous rivers. Landslide-derived sediment causes aggradation of riverbeds, which in turn leads to increased flooding that persists long after the earthquake, as rivers gradually evacuate the sediment[5–8]. Fluvial evacuation of landslide debris also affects mountain building, by facilitating erosion and mass removal, and influences the global carbon cycle, by changing erosional conditions that control carbon fluxes[3,9–13]. Despite this wide-ranging importance, gaps remain in quantifying the transport of sediment from earthquake-triggered landslides.

Hillslope sediment production during and after earthquakes has been well-characterized by mapping co- and post-seismic landslides, and their evolution with time[14–16]. Meanwhile, studies of river sediment fluxes after earthquakes have documented the removal of this material, most notably after the 1999 M_w7.7 (where M_w is the moment magnitude) Chi-Chi and 2008 M_w7.9 Wenchuan earthquakes. But these studies have only captured the suspended load through hydrological gauging[3,17]. Rivers transport sediment as both suspended load and bedload, and direct measurements of the bedload flux after earthquakes remain lacking. Suspended load is predominantly fine particles that represent a minor proportion of landslide material[18]. We expect that the coarse fraction of landslide debris is mainly transported as bedload—rolling and saltating particles near the riverbed—which is difficult to measure[4,19,20]. As a result, system-scale understanding of sediment dynamics after earthquakes is incomplete: we know how parts of the system evolve but cannot complete the budget without data on the bedload component.

Studies that have considered post-earthquake bedload dynamics have been inconclusive[4,5,19,21–23]. Field measurements of aggradation in channels and valleys after important earthquakes suggest that sediment evacuation can take from tens to several hundred years[5,23]. Model results differ markedly depending on the treatment of how channel morphology changes after input of landslide debris[4,19,21,22]. Adding to complexity, transport of landslide material can be influenced by region-specific conditions, such as lithology, climate, hydrology and vegetation[18,24–26].

Here we quantify sediment fluxes associated with bedload transport after the 2008 Wenchuan earthquake by taking advantage of a reservoir built just before the earthquake and located downstream of

[1]Department of Earth Science, University of California, Santa Barbara, CA, USA. [2]Department of Earth Sciences, University of Southern California, Los Angeles, CA, USA. [3]Division of Geological and Planetary Sciences, California Institute of Technology, Pasadena, CA, USA. [4]State Key Laboratory of Loess Science, Institute of Earth Environment, Chinese Academy of Sciences, Xi'an, China. [5]Institute of Global Environmental Change, Xi'an Jiaotong University, Xi'an, China. [6]Department of Geography, Chang'an University, Xi'an, China. [7]School of Geophysics and Geomatics, China University of Geosciences, Wuhan, China. [8]The Institute for Advanced Study of Coastal Ecology, Ludong University, Yantai, China. [9]Institute of Hazard, Risk and Resilience and Department of Geography, Durham University, Durham, UK. [10]Department of Earth Sciences, University of Oxford, South Parks Road, Oxford, UK. [11]School of Sustainable Energy and Resources, Nanjing University, Suzhou, China. [12]Woodwell Climate Research Center, Falmouth, MA, USA. ✉e-mail: ligen@ucsb.edu

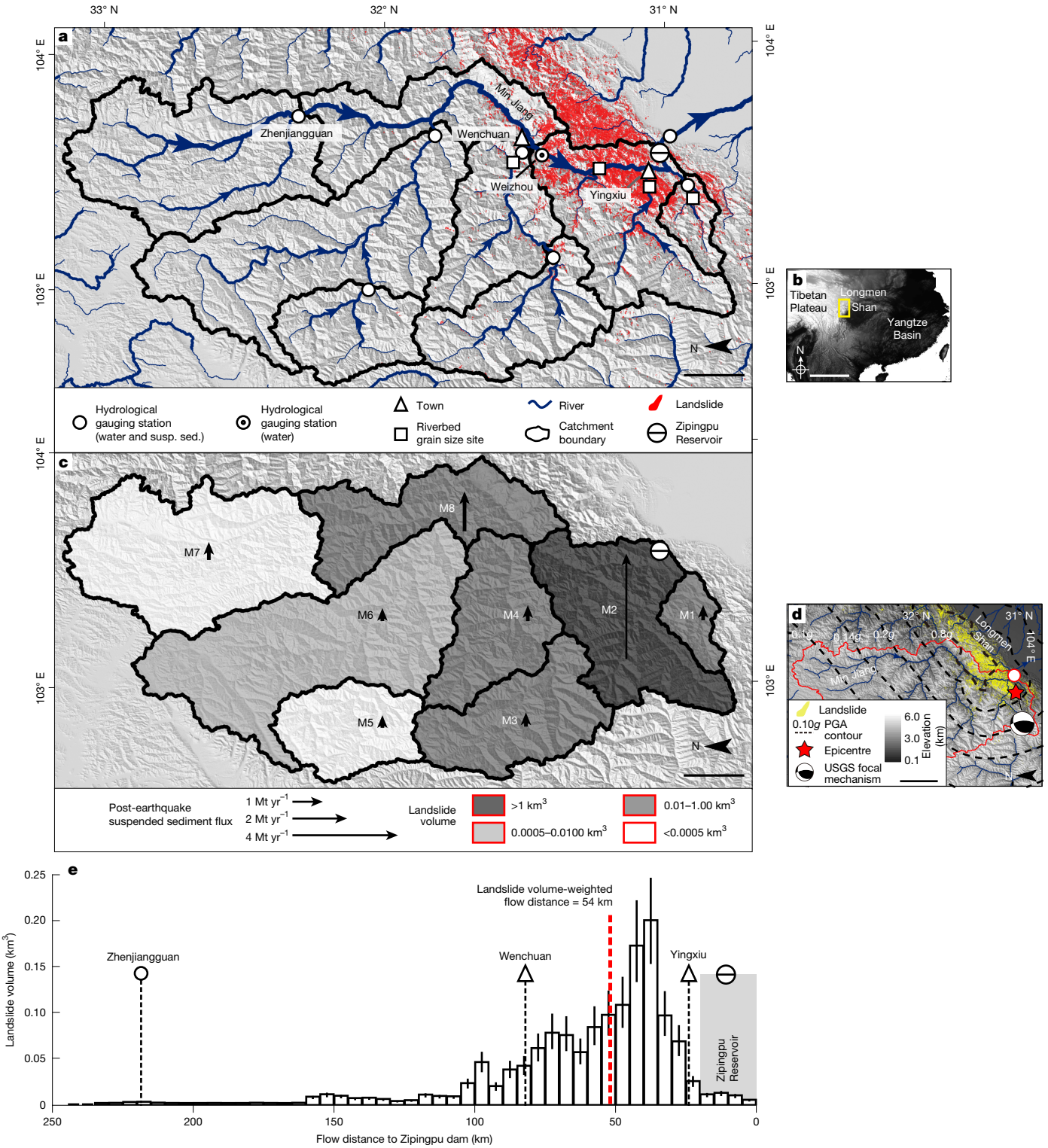

Fig. 1 | Map view and longitudinal profile of landslides and sediment fluxes in the Min Jiang basin. Map view of the Min Jiang basin. **a**, Shaded relief map of the Min Jiang basin, overlain by the locations of Zipingpu Reservoir, the hydrological gauging stations and corresponding catchments, the riverbed grain size study sites and co-seismic landslides triggered by the Wenchuan earthquake (in red). **b**, The regional context of the study area. **c**, Shaded relief map of the Min Jiang basin with sub-catchments M1–M7 shaded by landslide volumes, showing post-earthquake suspended sediment flux (arrows). **d**, The Min Jiang basin showing PGA (peak ground accelerations) contours and landslide polygons (yellow) along with the epicentre of the 2008 M_w7.9 Wenchuan earthquake. **e**, Total co-seismic landslide volume distributions along the flow distance to the Zipingpu dam (columns indicate medians of landslide volumes; bars indicate the 16th to 84th percentiles from Monte Carlo simulations). In **e**, for each landslide polygon, we calculated the average flow distance to the dam for all pixels in that landslide polygon. We then grouped all the landslides in the Min Jiang basin by their flow distance to the dam in 5 km increments and calculated landslide volumes in each bin. Scale bars, 20 km (**a**,**c**); 400 km (**b**); 40 km (**d**).

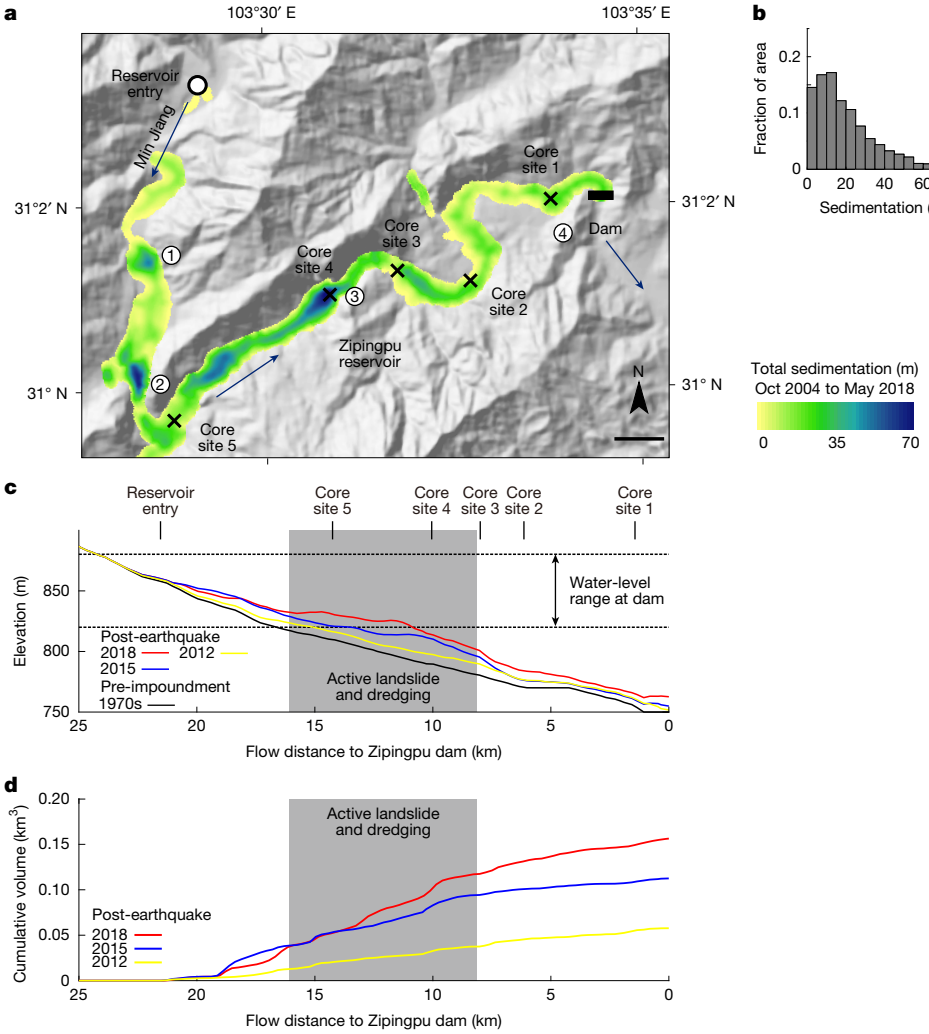

Fig. 2 | Map of sedimentation in Zipingpu Reservoir. Sediment accumulation in Zipingpu Reservoir. **a**, Shaded relief map of the Zipingpu Reservoir region with the colour-coded sedimentation map over the reservoir area (smoothed over 3-pixel-radius windows) in May 2018. **b**, Histogram of sedimentation thickness within the reservoir area after the 2018 survey. **c**, Longitudinal profile of the reservoir bed before reservoir impoundment (black curve) and of the average sediment thickness across the width of the valley during the survey timespan (colour curves), smoothed over a 4,000-m-wide moving window. **d**, Cumulative sediment volume calculated in 250-m increments along the flow distance. Landslide and human dredging activities were identified between core sites 3 and 5 (Extended Data Fig. 1b). The dashed lines in **c** indicate the range of water level measured at the dam[24], which covers much of the range of topographic elevation within the reservoir. Thus, subaerial fluvial entrainment and transport probably occurred across much of the deposited sediment in the reservoir, which may, in part, explain the irregular and time-evolving shapes seen in the profiles. Sedimentation patterns of other surveys are presented in Extended Data Fig. 1. Scale bar, 1 km (**a**).

the epicentral region. This reservoir trapped landslide-sourced sediment following the earthquake, allowing us to produce a source-to-sink budget and directly quantify the post-earthquake bedload flux from a study site near the source of landslide sediment. We combine measurements of sediment accumulation in the reservoir, grain sizes and suspended loads that entered and left the reservoir, to isolate the bedload component. We complement these measurements with the analysis of the grain size of river sediment and landslide deposits to establish a source-to-sink budget of sediment associated with a large earthquake.

Settings

The M_w7.9 Wenchuan earthquake occurred on 12 May 2008 in the Longmen Shan mountain range, central China[27]. The Longmen Shan marks the eastern margin of the Tibetan Plateau, featuring steep topography and active seismicity[28]. The regional climate is controlled by the East Asian monsoon, and more than 90% of annual precipitation occurs in the monsoon season (May–October) (ref. 28). With a recurrence interval of 500–4,000 years, the Wenchuan earthquake ruptured the Longmen Shan fault system[29,30]. This earthquake induced more than 60,000 landslides, which generated a total of about 3 km^3 of debris[12,31,32]. After the earthquake, landslides fed large quantities of sediment to rivers[17,33]. In this study, we focus on the Min Jiang basin, where around half of the Wenchuan landslides (by volume) occurred[31]. The Min Jiang drains into the man-made Zipingpu Reservoir (impounded in September 2004) at the Longmen Shan mountain front[24] (Fig. 1). Regulated by dam operation, the water level at the dam varies between 820 m and 880 m above sea level with high levels in October to January and low levels in March to May (ref. 24) (Fig. 2). Sediment is released from the reservoir mostly through sluicing.

Sediment accumulation in the reservoir

We conducted acoustic surveys in the reservoir in April 2012, May 2015 and May 2018 to quantify post-earthquake sediment accumulation. We also took sediment cores and measured sediment porosity to convert

sediment volume to mass. Our acoustic survey results indicated significant sediment accumulation in Zipingpu Reservoir following its impoundment. By May 2018, a total of 0.16 ± 0.01 km^3 sediment had accumulated in the reservoir, with only 0.014 ± 0.003 km^3 from before the Wenchuan earthquake (Methods). Between impoundment and May 2018, the total accumulated sediment thickness in the reservoir clustered around 10 m but showed a broad range across the reservoir, with local deposition of more than 60 m (Fig. 2a). The spatial pattern of sedimentation is related to the flow path of the Min Jiang River and the bathymetry of the reservoir. Four main deposition zones appear (1) where the river channel widens as it enters the reservoir; (2) upstream of a prominent constriction in the river valley; (3) in the central portion of the reservoir next to an active landslide complex (Extended Data Fig. 1b); and (4) just upstream of the dam (Fig. 2). Although the overall sedimentation patterns are generally consistent over the three surveys in 2012, 2015 and 2018 (Fig. 2b,c), longitudinal profiles show cumulative aggradation and progradation of sediment into the reservoir over the survey timespan as well as variations in local deposition rates (Fig. 2b). Some irregular topographic features in the sediment accumulation map and the longitudinal profile (for example, near core site 4, Fig. 2a) were probably caused by local landslide deposits, anthropogenic dredging and dynamic cut–fill cycles because of the fluctuating water level[24].

The total sediment volume accumulated in the reservoir increased linearly over the 10-year timespan of our surveys, from 0.06 ± 0.01 km^3 in April 2012 to 0.11 ± 0.01 km^3 in May 2015 and 0.16 ± 0.01 km^3 in May 2018 (Fig. 2, with all results here and below reported as mean ± 1σ or the medians and 16th to 84th percentiles of Monte Carlo simulations; Supplementary Information). The total post-earthquake sediment accumulation rate was 0.0162 ± 0.0006 km^3 yr^{-1} for 2012–2018 (Fig. 2), compared with a pre-earthquake rate of 0.0040 ± 0.0010 km^3 yr^{-1} (Methods). Some co-seismic landslides directly entered the reservoir (Extended Data Fig. 1b); these amount to 0.011–0.020 km^3 in total, making up approximately 14% of the total sediment mass in the reservoir in May 2018 (Methods). Therefore, the sediment budget in the reservoir was dominated by fluvial sediment input after the earthquake (Fig. 2).

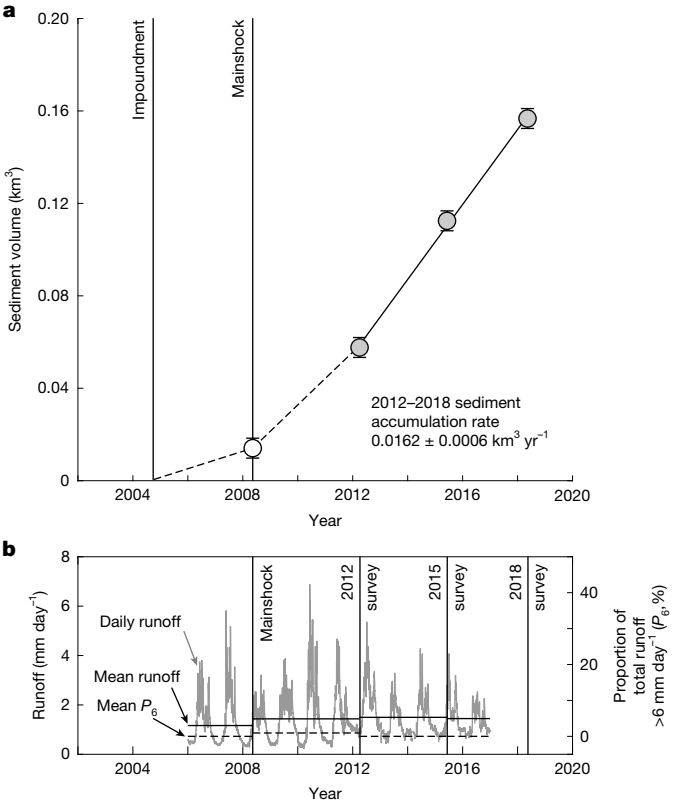

Fig. 3 | Sediment volumes in Zipingpu Reservoir over time. Changes of sediment volume in the reservoir and runoff of the Min Jiang mainstem measured upstream of the reservoir. **a**, Measured sediment volumes in the reservoir over time (filled circles and error bars, sediment volume; vertical lines, timing of reservoir impoundment and the Wenchuan earthquake mainshock; solid black line, best fit to the volume data through least-squares regression; open circle and error bars, sediment volume accumulated before the earthquake; Methods; dashed lines, inferred sedimentation before the first survey in 2012). **b**, Daily runoff (grey curves), mean runoff (black solid lines) and mean proportion of total runoff from high-magnitude events (>6 mm day^{-1}, black dashed lines) or P_6 averaged over the multi-year timespans between reservoir surveys of the Min Jiang mainstem at the Weizhou hydrologic gauging station upstream of the reservoir (Supplementary Fig. 1).

Post-earthquake sediment budget

The sediment deposited in the reservoir was transported there as both suspended load and bedload. We quantified the amount of suspended sediment that had been trapped in the reservoir after the earthquake by constraining the suspended sediment entering and leaving the reservoir separately using hydrological gauging datasets[17] (Methods). We calculated that, after the earthquake, the suspended sediment flux entering the reservoir was $9.14^{+3.43}_{-2.15}$ Mt yr^{-1}, of which $2.20^{+0.90}_{-0.88}$ Mt yr^{-1} left the reservoir (Methods). The difference between the suspended sediment fluxes entering and leaving the reservoir represents a suspended sediment accumulation rate in the reservoir of $7.02^{+3.53}_{-2.35}$ Mt yr^{-1}, equivalent to a retention rate of about 77% and a volumetric accumulation rate of $0.0077^{+0.0048}_{-0.0029}$ km^3 yr^{-1}, after accounting for porosity (Methods).

We assumed that only suspended sediment was released from the reservoir and determined the post-earthquake bedload flux as the difference between the suspended sediment accumulation rate and the total sediment accumulation rate. The volumetric bedload accumulation rate was $0.0085^{+0.0030}_{-0.0048}$ km^3 yr^{-1}, which translates into a bedload flux of $16.34^{+6.47}_{-9.25}$ Mt yr^{-1} after correcting for porosity. Adding the suspended sediment entering the reservoir to the bedload, we obtained a total sediment flux of $25.60^{+5.11}_{-6.65}$ Mt yr^{-1} and determined a bedload mass fraction (bedload: total sediment load) of 65^{+12}_{-26}% for the Min Jiang after the earthquake (Methods). There was minor anthropogenic dredging in the upstream part of the reservoir (Fig. 2b) and gravel bar development downstream of the dam, which suggests some bedload release from the reservoir (Supplementary Information). These factors would slightly increase the bedload estimates, but we expect their influence to be limited (Methods).

Compared with pre-earthquake levels, the total Min Jiang sediment flux increased by $5.7^{+1.3}_{-1.5}$ times after the earthquake, with the suspended load increasing by a modest $2.3^{+0.9}_{-0.6}$ times and the bedload increasing by a remarkable $27.4^{+14.6}_{-15.6}$ times (Fig. 4a). Our obtained post-earthquake bedload fraction (65^{+12}_{-26}%) is much higher than the pre-earthquake fraction (9.9–16.7%, determined from measured suspended: bedload ratios[28,34–36]) in the Min Jiang. The pre-earthquake bedload fraction falls close to a global trend between bedload fraction and drainage area for mountainous catchments[37], but the post-earthquake bedload fraction is markedly higher (Fig. 4b), highlighting the prominent effect of localized sediment sources in bedload transport (Fig. 1c).

High bedload flux after the Wenchuan event

Our sediment budget (Fig. 3) highlights the potential for bedload to sustain heightened sediment transport after large earthquakes over decadal timescales[4], and the increased bedload fraction (Fig. 4) indicates that the Min Jiang shifted to a bedload-dominated system following the Wenchuan earthquake. We interpret this shift to have been driven by the supply of coarse material from hillslopes, accentuated by coarse sediment armouring river beds and protecting fine sediment

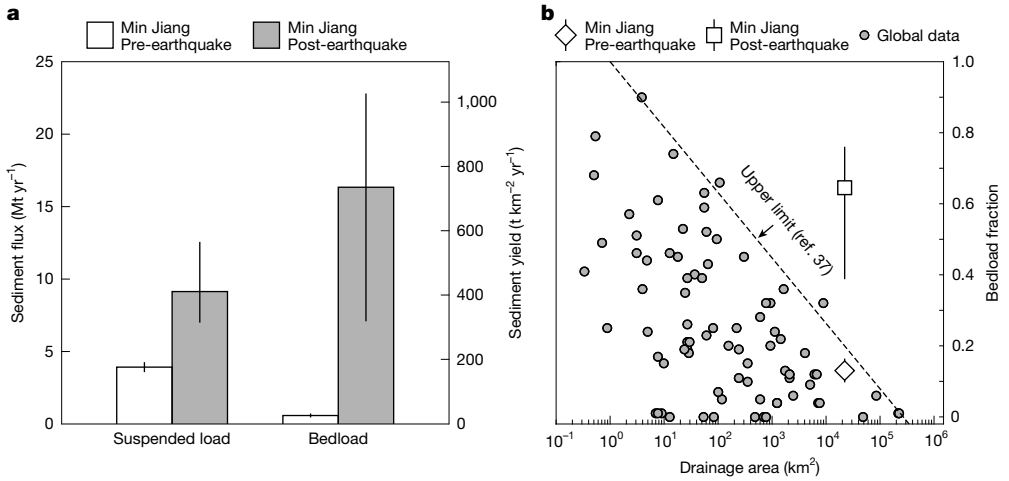

Fig. 4 | Sediment load and bedload fraction before and after the Wenchuan earthquake. Sediment flux, sediment yield and bedload fraction of the Min Jiang River before and after the Wenchuan earthquake. **a**, Comparison of suspended load and bedload fluxes and related sediment yields before and after the earthquake. **b**, Bedload fraction (by mass) before and after the earthquake in the context of a global dataset of mountainous, gravel-bedded rivers[37], showing how bedload fraction varies with drainage area. The dashed line indicates an empirical upper limit[37], notably exceeded in the Min Jiang after the Wenchuan earthquake. The drainage area is taken where the Min Jiang enters the Zipingpu Reservoir. All error bars represent the 16th to 84th percentiles of the Monte Carlo results.

from entrainment[38]. This finding is corroborated by observations from satellite imagery showing aggradation and storage of landslide material in the upstream channel network[16]. The relatively short distance (landslide volume-weighted flow distance of about 54 km; Fig. 1c) between the reservoir and landslide inputs distributed along the mainstem may have limited abrasion that converts bedload to finer sediment[7], allowing bedload to dominate the reservoir sedimentation.

Based on the total sediment flux and a reported dissolved:suspended load ratio of 19 ± 7% for the post-earthquake period[29], we estimate that, within 10 years after the earthquake, around $8.7^{+3.5}_{-2.8}$% of the total co-seismic landslide mass in the Min Jiang catchment had been exported by the river system (Supplementary Information). Other studies have mapped spatiotemporal changes in hillslope and channel deposits in parts of the Min Jiang catchment and estimated that about 12% of the co-seismic landslide volume in the catchment has been delivered to the Min Jiang mainstem over similar timescales[16,39]. These estimates of hillslope-to-channel sediment delivery slightly exceed, yet broadly align with, our calculated sediment delivery to the reservoir, suggesting that the Min Jiang is capable of exporting most landslide sediment delivered to the mainstem.

Enhanced and sustained bedload transport

Shear stress calculations using pre-earthquake channel geometry estimated much lower bedload transport capacity in the Min Jiang mainstem (around 1.73 Mt yr^{-1}) (ref. 22) than calculated from our direct observations ($16.34^{+6.47}_{-9.25}$ Mt yr^{-1}). Higher transport rates should be expected after the earthquake because of abundant sediment supply that can produce unstable channel beds[40] and highly dynamic riverbed topography, causing locally narrowed and steepened channel threads that increase local bed stresses[19]. To constrain changes in channel morphology, we measured channel widths from 2006 to 2019 at 80 sites, where landslides connect to Min Jiang (Methods). Landslides narrowed the width of the Min Jiang channel by an average of about 30% (Extended Data Fig. 3), supporting that the interplay between landslides and channel geometry can contribute to increasing sediment transport capacity after a major earthquake[19]. High sediment transport rates could also be facilitated by suspended sand and gravel[41], as well as debris flows and hyper-concentrated flows[42], given the steep channel-bed gradients (around 1%; Fig. 2c) upstream of the reservoir.

Considering a total material transport flux as the sum of sediment and dissolved fluxes, the debris from Wenchuan-triggered landslides could be evacuated over approximately 100–200 years under the current transport rates (Supplementary Information). However, several factors complicate prediction of sediment transport fluxes in the future. Landslide debris contains abundant coarse materials, which some studies have suggested may be difficult for rivers to entrain and transport[17,18]. However, our field observations suggest that Min Jiang can entrain and transport most or all of the sediment from landslide deposits, because surface riverbed materials, the coarser portion of river-carried particles, have coarser grains than landslide deposits (Extended Data Fig. 4a). We also observed that the Min Jiang delivered coarse particles from gravels to metre-sized boulders into the reservoir (Extended Data Fig. 2). Moreover, subsurface riverbed materials have generally finer particle sizes than landslide debris (Extended Data Fig. 4b), probably resulting from abrasion[7] and/or sorting[18], which would facilitate fluvial removal of this material. However, landslide material could remain stored in headwater catchments[5], delaying its delivery to the Min Jiang main stem. Delivery of landslide debris to channels may also be limited by revegetation of failed hillslopes, which would stabilize deposits[43].

Climatic conditions could also affect the supply of landslide debris to rivers and subsequent transport[19]. Monsoonal precipitation can enhance the transport of landslide material by inducing debris flows, which facilitate delivery of sediment from low-order to high-order channels[39,44,45]. Although we see a near-constant post-earthquake sediment accumulation rate over the multi-year duration of our reservoir surveys, sedimentation in Zipingpu Reservoir varies inter-annually depending on hydrological conditions[24]. These hydrological variations are dampened when averaged over our survey intervals (3–4 years) (Fig. 3b), but are likely to be important for sediment transport over the long term. Models predict increased frequency of extreme precipitation events in the study area in the next 50 years (ref. 25), suggesting the potential for enhanced landslide sediment delivery to channels and increased sediment flux[4,46]. Continued monitoring will be required to determine the combined effect of geomorphic processes, vegetation dynamics and climatic conditions on the transport of landslide debris over the coming decades.

Our observations show that bedload can dominate river sediment flux after major earthquakes. This bedload transport facilitates the efficient fluvial transport of landslide-derived sediment, implying that

evacuation of landslide debris from mountains is limited primarily by sediment delivery from hillslopes into and through low-order channels. The seismically enhanced bedload flux may dissipate downstream because of abrasion[7], which will depend on transport distance and sediment erodibility[7,47]. For example, there is much less pronounced bedload transport in major trans-Himalayan rivers than in our study[7], which, at first glance, contrasts with our results, given that co-seismic landslides are also an important sediment source in the Himalayas[48]. However, the landslides induced by the 2015 Gorkha Earthquake—a prominent recent event in the Himalayas—are located 250–300 km (weighted by landslide volume) upstream of the mountain front, much longer than the approximately 54 km distance for the Min Jiang (Fig. 1e and Extended Data Fig. 5). Furthermore, about 70% of the landslide volume in the Min Jiang basin is associated with granitic rocks (Supplementary Information), which are characterized by lower abrasion rates than sediments derived from Himalayan rocks[18,49]. In many other seismically active regions, we expect transport distances from landslides to mountain fronts of the order of 10 s of km—such as in New Zealand, Taiwan and southern California[4,5,50]. Therefore, the main role for post-earthquake bedload transport—and associated cascading hazards—may be expected in these landscapes, especially where rocks produce coarse landslide debris and have low erodibility[7,47,49]. Our results emphasize how earthquakes close to mountain fronts can markedly elevate bedload sediment supply to adjacent plains on decadal timescales, generating fluvial hazards that persist long after the shaking stops and in areas far beyond the epicentral region.

Online content

Any methods, additional references, Nature Portfolio reporting summaries, source data, extended data, supplementary information, acknowledgements, peer review information; details of author contributions and competing interests; and statements of data and code availability are available at https://doi.org/10.1038/s41586-025-09354-8.

1. Keefer, D. K. Landslides caused by earthquakes. *Geol. Soc. Am. Bull.* **95**, 406–421 (1984).
2. Keefer, D. K. Investigating landslides caused by earthquakes – a historical review. *Surv. Geophys.* **23**, 473–510 (2002).
3. Hovius, N. et al. Prolonged seismically induced erosion and the mass balance of a large earthquake. *Earth Planet. Sci. Lett.* **304**, 347–355 (2011).
4. Yanites, B. J., Tucker, G. E., Mueller, K. J. & Chen, Y.-G. How rivers react to large earthquakes: evidence from central Taiwan. *Geology* **38**, 639–642 (2010).
5. Pearce, A. J. & Watson, A. J. Effects of earthquake-induced landslides on sediment budget and transport over a 50-yr period. *Geology* **14**, 52–55 (1986).
6. Fan, X. et al. Earthquake-induced chains of geologic hazards: Patterns, mechanisms, and impacts. *Rev. Geophys.* **57**, 421–503 (2019).
7. Dingle, E. H., Attal, M. & Sinclair, H. D. Abrasion-set limits on Himalayan gravel flux. *Nature* **544**, 471–474 (2017).
8. Chen, C.-Y. Sedimentary impacts from landslides in the Tachia River Basin, Taiwan. *Geomorphology* **105**, 355–365 (2009).
9. Densmore, A. L. et al. Reply to 'Isostasy can't be ignored'. *Nat. Geosci.* **5**, 83–84 (2012).
10. Emberson, R., Hovius, N., Galy, A. & Marc, O. Chemical weathering in active mountain belts controlled by stochastic bedrock landsliding. *Nat. Geosci.* **9**, 42–45 (2016).
11. Frith, N. V. Carbon export from mountain forests enhanced by earthquake-triggered landslides over millennia. *Nat. Geosci.* **11**, 772–776 (2018).
12. Parker, R. N. et al. Mass wasting triggered by the 2008 Wenchuan earthquake is greater than orogenic growth. *Nat. Geosci.* **4**, 449–452 (2011).
13. Wang, J. et al. Long-term patterns of hillslope erosion by earthquake-induced landslides shape mountain landscapes. *Sci. Adv.* **6**, eaaz6446 (2020).
14. Marc, O., Hovius, N., Meunier, P., Uchida, T. & Hayashi, S. Transient changes of landslide rates after earthquakes. *Geology* **43**, 883–886 (2015).
15. Fan, X. et al. Spatio-temporal evolution of mass wasting after the 2008 Mw 7.9 Wenchuan earthquake revealed by a detailed multi-temporal inventory. *Landslides* **15**, 2325–2341 (2018).
16. Francis, O. et al. The fate of sediment after a large earthquake. *J. Geophys. Res. Earth Surface* **127**, e2021JF006352 (2022).
17. Wang, J. et al. Controls on fluvial evacuation of sediment from earthquake-triggered landslides. *Geology* **43**, 115–118 (2015).
18. Attal, M. & Lavé, J. Changes of bedload characteristics along the Marsyandi River (central Nepal): implications for understanding hillslope sediment supply, sediment load evolution along fluvial networks, and denudation in active orogenic belts. *Geol. Soc. Am. Special Pap.* **398**, 143–171 (2006).
19. Croissant, T., Lague, D., Steer, P. & Davy, P. Rapid post-seismic landslide evacuation boosted by dynamic river width. *Nat. Geosci.* **10**, 680–684 (2017).
20. Cook, K. L., Andermann, C., Gimbert, F., Adhikari, B. R. & Hovius, N. Glacial lake outburst floods as drivers of fluvial erosion in the Himalaya. *Science* **362**, 53–57 (2018).
21. Croissant, T. et al. Seismic cycles, earthquakes, landslides and sediment fluxes: linking tectonics to surface processes using a reduced-complexity model. *Geomorphology* **339**, 87–103 (2019).
22. Liu, F., Fu, B. & Yang, S. Quantitative estimation of the evacuation time of landslide mass and sediment induced by the great events like 2008 Wenchuan earthquake along the Min Jiang River, Longmen Shan orogenic belt. *Chin. J. Geophys.* **56**, 1517–1525 (2013).
23. Stolle, A. et al. Protracted river response to medieval earthquakes. *Earth Surf. Processes Landforms* **44**, 331–341 (2019).
24. Zhang, F. et al. Monsoonal control on a delayed response of sedimentation to the 2008 Wenchuan earthquake. *Sci. Adv.* **5**, eaav7110 (2019).
25. Li, C., Wang, M., Liu, K. & Coulthard, T. J. Landscape evolution of the Wenchuan earthquake-stricken area in response to future climate change. *J. Hydrol.* **590**, 125244 (2020).
26. Lin, W.-T., Lin, C.-Y. & Chou, W.-C. Assessment of vegetation recovery and soil erosion at landslides caused by a catastrophic earthquake: A case study in Central Taiwan. *Ecol. Eng.* **28**, 79–89 (2006).
27. Burchfiel, B. C. A geological and geophysical context for the Wenchuan earthquake of 12 May 2008, Sichuan, People's Republic of China. *GSA Today* **18**, 4–11 (2008).
28. Liu-Zeng, J., Wen, L., Oskin, M. & Zeng, L. S. Focused modern denudation of the Longmen Shan margin, eastern Tibetan Plateau. *Geochem. Geophys. Geosyst.* **12**, Q11007 (2011).
29. Li, G. et al. Earthquakes drive focused denudation along a tectonically active mountain front. *Earth Planet. Sci. Lett.* **472**, 253–265 (2017).
30. Shen, Z.-K. et al. Slip maxima at fault junctions and rupturing of barriers during the 2008 Wenchuan earthquake. *Nat. Geosci.* **2**, 718–724 (2009).
31. Li, G. et al. Connectivity of earthquake-triggered landslides with the fluvial network: implications for landslide sediment transport after the 2008 Wenchuan earthquake. *J. Geophys. Res. Earth Surface* **121**, 703–724 (2016).
32. Li, G. et al. Seismic mountain building: landslides associated with the 2008 Wenchuan earthquake in the context of a generalized model for earthquake volume balance. *Geochem. Geophys. Geosyst.* **15**, 833–844 (2014).
33. West, A. J. et al. Dilution of 10Be in detrital quartz by earthquake-induced landslides: Implications for determining denudation rates and potential to provide insights into landslide sediment dynamics. *Earth Planet. Sci. Lett.* **396**, 143–153 (2014).
34. Chen, J. Y. & Hu, C. Y. Sediment transport rate and characteristics of gravel bed-load at Dujiangyang. *J. Sediment Res.* **4**, 22–29 (1985).
35. Qu, Z. *Study on Mechanics of Gravel Movement in Minjiang River*. MS thesis, Tsinghua Univ. (1998).
36. Xu, M. J. Sediment study at Dujiang Yang. *Sediment Res.* **1**, 42–57 (1981).
37. Turowski, J. M., Rickenmann, D. & Dadson, S. J. The partitioning of the total sediment load of a river into suspended load and bedload: a review of empirical data. *Sedimentology* **57**, 1126–1146 (2010).
38. Parker, G. & Toro-Escobar, C. M. Equal mobility of gravel in streams: the remains of the day. *Water Resour. Res.* **38**, 46-41–46-48 (2002).
39. Fan, X. et al. Two multi-temporal datasets that track the enhanced landsliding after the 2008 Wenchuan earthquake. *Earth Syst. Sci. Data* **11**, 35–55 (2019).
40. Masteller, C. C., Finnegan, N. J., Turowski, J. M., Yager, E. M. & Rickenmann, D. History-dependent threshold for motion revealed by continuous bedload transport measurements in a steep mountain stream. *Geophys. Res. Lett.* **46**, 2583–2591 (2019).
41. de Leeuw, J. et al. Entrainment and suspension of sand and gravel. *Earth Surf. Dyn.* **8**, 485–504 (2020).
42. Rickenmann, D. Hyperconcentrated flow and sediment transport at steep slopes. *J. Hydraul. Eng.* **117**, 1419–1439 (1991).
43. Yang, W., Qi, W. & Zhou, J. Decreased post-seismic landslides linked to vegetation recovery after the 2008 Wenchuan earthquake. *Ecol. Indic.* **89**, 438–444 (2018).
44. Dahlquist, M. P. & West, A. J. Initiation and runout of post-seismic debris flows: insights from the 2015 Gorkha Earthquake. *Geophys. Res. Lett.* **46**, 9658–9668 (2019).
45. Theule, J. I., Liébault, F., Loye, A., Laigle, D. & Jaboyedoff, M. Sediment budget monitoring of debris-flow and bedload transport in the Manival Torrent, SE France. *Nat. Hazards Earth Syst. Sci.* **12**, 731–749 (2012).
46. Xie, J., Wang, M., Liu, K. & Coulthard, T. J. Modeling sediment movement and channel response to rainfall variability after a major earthquake. *Geomorphology* **320**, 18–32 (2018).
47. Attal, M. & Lavé, J. Pebble abrasion during fluvial transport: experimental results and implications for the evolution of the sediment load along rivers. *J. Geophys. Res. Earth Surface* **114**, F04023 (2009).
48. Marc, O. et al. Long-term erosion of the Nepal Himalayas by bedrock landsliding: the role of monsoons, earthquakes and giant landslides. *Earth Surf. Dyn.* **7**, 107–128 (2019).
49. Godard, V. et al. Spatial distribution of denudation in Eastern Tibet and regressive erosion of plateau margins. *Tectonophysics* **491**, 253–274 (2010).
50. Harp, E. L. & Jibson, R. W. Landslides triggered by the 1994 Northridge, California, earthquake. *Bull. Seismol. Soc. Am.* **86**, S319–S332 (1996).

Methods

Acoustic surveys and reservoir sedimentation estimates

To measure sediment accumulation in Zipingpu Reservoir, we conducted acoustic surveys to scan the reservoir in May 2012, April 2015 and May 2018, and we collected 1-m-long sediment cores in May 2012 (Extended Data Fig. 1). Another 10.89-m-long sediment core was retrieved from the reservoir in October 2016, producing a record of sedimentation and its temporal variability at one site[24]. Here, we complemented that long record and provided the reservoir-wide perspective that allows for estimating total sediment volume. We measured the porosity of the sediment from cores at multiple sites across the reservoir, yielding a range of 0.41–0.90, with an average of 0.65 ± 0.08 (±1σ, n = 288; Supplementary Table 3). Measured porosities were used to convert sediment volumes to sediment mass (Supplementary Text 8).

To process the acoustic reflection profiles, we developed an automated picking algorithm to identify the sediment–water interface. We then delineated reservoir bathymetry at each survey time point and compared the bathymetry with the topography before the impoundment of the reservoir (Supplementary Information). We used the differences in bathymetry to estimate the volume of sediment sequestered in the reservoir between each survey. The uncertainties in sediment volumes are propagated from the instrumental errors, the error of the pre-impoundment digital elevation model and the uncertainties in the extrapolation from the surveyed transects. Further technical details are provided in the Supplementary Information.

Suspended sediment budget

To estimate the suspended sediment fluxes entering and leaving the reservoir, we analysed the water and sediment discharge datasets collected by 17 hydrological gauging stations of the Chinese Bureau of Hydrology (CBH) across the Longmen Shan[17] (Supplementary Fig. 2) and constructed suspended sediment budgets. The 17 stations are located in three main river basins draining the Longmen Shan: Min Jiang, Tuo Jiang and Fujiang, with nine in the Min Jiang basin (eight in the mountains and one in the lowland plain). The eight montane stations segregated the Min Jiang basin (above the Zipingpu Reservoir) into eight sub-catchments (M1–M8) but two sub-catchments (M2 and M8) lacked suspended sediment data (Fig. 1 and Supplementary Fig. 1). Here we present a summary of our approach to estimating suspended sediment fluxes entering the reservoir using these data, with more details provided in Supplementary Text 7 and Supplementary Figs. 8–10. We adopted Monte Carlo random sampling simulations to propagate uncertainties from different parameters, and we report results as medians and 16th to 84th percentiles of the Monte Carlo results.

For the pre-earthquake period, we used the average suspended sediment yield in the gauged sub-catchments to approximate the suspended sediment yield in M2 and M8, and summed suspended sediment fluxes in M1–M8 to estimate a total suspended sediment flux entering the reservoir as 3.40 ± 0.37 Mt yr^{-1}.

For the post-earthquake period, previous studies found that the post-earthquake suspended sediment yields (t km^2 yr^{-1}) in the Longmen Shan catchments were controlled by landslide volumes and the number of high-magnitude (runoff >6 mm day^{-1}) water discharge events[17,29]. Thus, we derived a two-parameter empirical relation between post-earthquake suspended sediment yield, landslide volume and an index for high-magnitude water discharge events (proportion of total runoff from >6 mm day^{-1} events) to predict the post-earthquake suspended sediment yield and flux in sub-catchments M2 and M8 (Supplementary Text S7 and Supplementary Fig. 10). This empirical relation is calibrated against other 11 catchments draining the Longmen Shan (Supplementary Text 7 and Supplementary Fig. 10). We used total landslide volumes instead of channel-connected landslide volumes because previous studies[31] showed that whether or not landslide-channel connectivity is considered, the landslide volume-suspended sediment yield correlations are statistically indistinguishable in the studied catchments, which may be related to the mobilization of fine sediment from landslides unconnected to channels. Using the resulting estimate for the suspended sediment flux from M2 and M8, we summed suspended sediment fluxes in M1–M8 to obtain a total post-earthquake suspended sediment fluxes entering the reservoir as $9.14^{+3.43}_{-2.15}$ Mt yr^{-1}.

We also estimated suspended sediment fluxes leaving the reservoir through mass balance calculations using the CBH dataset as 0.52 ± 0.14 Mt yr^{-1} and $2.20^{+0.90}_{-0.88}$ Mt yr^{-1} for the pre-earthquake and post-earthquake periods, respectively (Supplementary Text 7 and Supplementary Figs. 8 and 11). The difference between the suspended sediment fluxes entering and leaving the reservoir determined the suspended sediment flux trapped in the reservoir (pre-earthquake: 3.40 ± 0.37 Mt yr^{-1}, post-earthquake: $7.02^{+3.53}_{-2.35}$ Mt yr^{-1}).

We note that other hydrological data sourced from the 1960s to 1980s have been used in other studies in the region[28]. However, since the late 1980s, the government has conducted large-scale water–soil conservation projects in the basin, which notably reduced the sediment load[51]. Thus, we chose not to use the 1960s to 1980s sediment data to estimate the pre-earthquake sediment load in this study.

Total sediment budget

We estimated the sediment volumetric accumulation rate (km^3 yr^{-1}) in the reservoir by correcting for porosity (Supplementary Text 8). We used the porosity of sediment core samples (0.65 ± 0.08) to approximate the porosity of suspended sediment deposited in the reservoir, given the similar grain sizes observed for suspended sediment[17,24]. A porosity of 0.10–0.41 was assigned for the porosity of bedload sediment deposited in the reservoir, where 0.41 was the lowest porosity measured in the samples and 0.10 was an assumed lower bound.

The pre-earthquake bedload flux was determined from the pre-earthquake suspended load (3.92 ± 0.35 Mt yr^{-1}, determined above) and the previously reported bedload: suspended load ratio of 11.7–20% (refs. 28,34–36). We obtained a bedload fraction (bedload:total sediment load) of 9.9–16.7%, a bedload flux of 0.58 ± 0.14 Mt yr^{-1} and a total sediment load of 4.51 ± 0.41 Mt yr^{-1} for the pre-earthquake period. We assumed that only suspended sediment was released from the dam, and thus all bedload was trapped in the reservoir (0.58 ± 0.14 Mt yr^{-1} with a porosity of 0.10–0.41), whereas the suspended sediment flux trapped in the reservoir was determined earlier as 3.40 ± 0.37 Mt yr^{-1} (with an approximated porosity of 0.65 ± 0.08) before the earthquake. Accounting for porosity, we resolved a pre-earthquake sediment accumulation rate of 0.0040 ± 0.0010 km^3 yr^{-1} and the total volume of sediment accumulated in the reservoir before the earthquake as 0.014 ± 0.003 km^3.

For the post-earthquake period, suspended sediment was trapped in the reservoir at a rate of $7.02^{+3.53}_{-2.35}$ Mt yr^{-1}, which translated into a volumetric rate of $0.0077^{+0.0048}_{-0.0029}$ km^3 yr^{-1} with correction for porosity (0.65 ± 0.08). The difference between the suspended sediment accumulation rate ($0.0077^{+0.0048}_{-0.0029}$ km^3 yr^{-1}) and the total volumetric accumulation rate (0.0162 ± 0.0006 km^3 yr^{-1}, determined from acoustic surveys) yielded a bedload volumetric accumulation rate of $0.0085^{+0.0030}_{-0.0048}$ km^3 yr^{-1}. Taking a porosity of 0.10–0.41, we resolved the bedload mass accumulation rate of $16.34^{+6.47}_{-9.25}$ Mt yr^{-1}. Assuming no bedload was released from the dam (see following section), we determined that the post-earthquake bedload flux delivered into the reservoir by Min Jiang was $16.34^{+6.47}_{-9.25}$ Mt yr^{-1}, whereas the post-earthquake Min Jiang suspended sediment flux was $9.14^{+3.43}_{-2.15}$ Mt yr^{-1} (see above). Combining the two fluxes, we calculated a post-earthquake bedload fraction of 65^{+12}_{-26}% and a total post-earthquake sediment load of $25.60^{+5.11}_{-6.65}$ Mt yr^{-1}. Combining the suspended load and bedload mass accumulation rates in the reservoir (Supplementary Texts 7 and 8 and Supplementary Figs. 8 and 9) and accumulation timespan (pre-earthquake: September 2004 to May 2008; post-earthquake: May 2008 to May 2018), we estimated a total sediment mass of about 249 Mt (corrected for porosity) in the reservoir till May 2018.

Total material transport flux was calculated as the sum of the suspended sediment flux, bedload flux and dissolved load flux. Dissolved load flux was calculated from previously reported dissolved:suspended load ratios (pre-earthquake: 19 ± 6%, ref. 28; post-earthquake: 19 ± 7%; ref. 29).

Bedload release from the dam

In the sediment budget calculations, we assumed no bedload release from the dam. However, we believe two processes caused some bedload loss from the reservoir. We ignored these processes in our calculations because we determined that they probably have limited influence on the sediment budget. Here we explain this rationale. First, two gravel bars developed within 1,800 m downstream of the dam after the earthquake, as visible in optical satellite imagery (Supplementary Fig. 13). These bars had a total area of around 26,000 m^2 (one was about 7,000 m^2 and the other was about 19,000 m^2, measured from Google Earth imagery). We determined a channel depth of around 13 m, adopting an empirical scaling between bankfull width and depth for gravel bed rivers[52] and a channel width of approximately 160 m measured from Google Earth imagery (Supplementary Text 9 and Supplementary Fig. 13). On this basis, the total volume of sediment in the two gravel bars was about 338,000 m^3 or 3.4×10^{-4} km^3 (26,000 $m^2 \times 13$ m), only around 0.2% of the total sediment trapped in the reservoir in 2018 (0.17 km^3). Second, during our surveys, we noticed dredging in the upstream region of the reservoir between core sites 3 and 5 (Fig. 2a). The dredging was localized (within a range of about 100 s m x 100 s m) and conducted on a small boat not equipped with large-scale dredging facilities. Given the contrasting spatial scales of the reservoir (about 16 km^2) compared with dredging (<0.1 km^2), we expect the dredging to have limited influence on the total sediment budget, although it could potentially modify local channel morphology (Fig. 2).

Landslide and riverbed grain size estimates

To evaluate how rivers transport different-sized particles from landslides, we assembled a grain size dataset of landslide and riverbed sediments from fieldwork and compilation of published data. We conducted field measurements (sieving and photometry) of the grain size of riverbed materials at four field sites (at the main Min Jiang channel at its entrance to the reservoir and at the outlets of three main tributaries, Fig. 1). To estimate the grain size distributions for landslide populations, we compiled data from published literature, supplemented these by our new field measurements and classified the data by lithology. We then predicted the grain size composition of other landslides based on lithology, following a previous study in the Himalayas[18]. We estimated combined size distributions for landslide populations using Monte Carlo random sampling simulations to account for uncertainties. The results were analysed together with a Wenchuan landslide inventory map and the gauging data of pre- and post-earthquake suspended sediment flux. The landslide volumes were calculated from landslide area–volume scaling relations and reported as the median and 16th to 84th percentiles of random sampling simulations to account for uncertainties in scaling parameters[31,32]. The landslide mass was calculated from the landslide volume by quantifying an overall porosity for landslide deposits (see Supplementary Text 9 for more technical details). We consider earthquake-induced landslides as the main source of coarse sediment in the system, which are the primary contributors to the long-term erosion budget of Longmen Shan[29] and have more abundant giant landslides than rainfall-induced landslides in the region[53].

Remote sensing analyses

To constrain the magnitude of sediment supplied by landslides within the reservoir region itself (that is, direct input of landslide debris into the reservoir from surrounding hillslopes), we constructed a digital elevation model (DEM) from 2021 stereoscopic satellite imagery (WorldView-2, Imagery 2021 Maxar) using a Surface Extraction with TIN-based Search-space Minimization algorithm[54,55]. We then compared the 2021 DEM to the pre-earthquake DEM to quantify the volume of material derived from the landslide-affected zones in the reservoir (Extended Data Fig. 1b and Supplementary Fig. 14). Because of the limited imagery available, we could derive only the elevation changes of the landslides that occurred on the valley walls between core sites 3 and 5 (Extended Data Fig. 1b). These are the largest landslides surrounding the reservoir as mapped in optical satellite imagery. We used the elevation changes derived from stereo imagery analysis to estimate a sediment loss of 0.015 km^3 from the reservoir-surrounding landslides covered by our DEM (Extended Data Fig. 1b), comparable to the total volume of those landslides estimated from landslide area–volume scaling relations ($0.011^{+0.003}_{-0.003}$ km^3; Supplementary Information). The estimated sediment loss (0.015 km^3) from those landslides, mostly from the landslide complex nearby core site 4 (Fig. 2d and Extended Data Fig. 1b), was comparable to the sediment accumulation around core site 4 in 2018 (about 0.01–0.02 km^3, Fig. 2d), providing a plausible explanation of the high sediment accumulation at this site (that is, zone 3 in Fig. 2a). For the landslides in the reservoir region beyond the extent of stereo imagery analysis, we estimated a total volume of $0.004^{+0.001}_{-0.001}$ km^3 from landslide area–volume scaling relations. Combining these results, we estimated a volume of 0.011–0.020 km^3 for sediment sourced from landslides that occurred in the reservoir region (Extended Data Fig. 1b and Supplementary Fig. 14). We assumed that this landslide material is mostly coarse-grained as the landslide complex is dominated by a large, deep-seated bedrock landslide. This volume translates into about 25–45 Mt of sediment after correcting for porosity (median porosity of landslide deposits around 0.15; Supplementary Text 10), making up about 10–18% (average 14%) of the total sediment mass in the reservoir in 2018 (approximately 249 Mt). We note that using the 2021 DEM may overestimate the landslide material entering the reservoir up to 2018 when we had the last acoustic survey, but we do not expect this time difference to cause fundamental changes to our estimated volumes of landslide material entering the reservoir, especially because the landslide scars did not show significant changes during this time.

To characterize the morphodynamic changes of the Min Jiang channel following the Wenchuan earthquake, we measured the widths of the Min Jiang channel at 80 sites at which the earthquake-triggered landslides connected to and entered the Min Jiang from 2006 to 2019 from satellite imagery accessed by Google Earth, supplemented by selected QuickBird, WorldView and IKONOS Imagery (2006–2008 Maxar; Extended Data Fig. 4 and Supplementary Table 6). We then normalized each channel width measurement to the pre-earthquake channel width, grouped the data into each individual year and calculated the medians and 16th to 84th percentiles of the normalized channel width for each year (Extended Data Fig. 4).

Data availability

The derived reservoir sedimentation data shown in Fig. 1 and Extended Data Fig. 1 are available at the Hydroshare data repository (http://www.hydroshare.org/resource/210dd056c15c45208de9b5ba6a75cc61). Datasets of grain size, reservoir core sediment porosity, hydrological variability, mapped channel width, landslide volumes, high-magnitude water discharge index and suspended sediment yield are in Supplementary Tables 1–7, which are also available at the Hydroshare data repository. The DEM data used for geospatial analysis were downloaded from SRTM 90m Digital Elevation Database v.4.1 provided by the CGIAR Consortium for Spatial Information[56]. DEM data were analysed and visualized using ArcMap 10.8 and TopoToolbox[57] in Matlab. The pre-impoundment DEM data were adopted from ref. 58. Landsat imagery was downloaded from the US Geological Survey EarthExplorer website (https://earthexplorer.usgs.gov/). SPOT imagery (SPOT 5 imagery 2008 CNES) was obtained from the SPOT imagery corporation (SICORP). Google Earth imagery was available at Google Earth Pro.

Code availability

The central function of the automated picking algorithm was adopted from the Python package 'obspy', available online (https://docs.obspy.org/packages/autogen/obspy.signal.trigger.classic_sta_lta.html). Custom Matlab codes for sediment budget calculations and relevant analyses are available at the Hydroshare data repository (http://www.hydroshare.org/resource/210dd056c15c45208de9b5ba6a75cc61).

51. Chen, X., Yan, Y., Fu, R., Dou, X. & Zhang, E. Sediment transport from the Yangtze River, China, into the sea over the Post-Three Gorge Dam Period: A discussion. *Quat. Int.* **186**, 55–64 (2008).
52. Parker, G., Wilcock, P. R., Paola, C., Dietrich, W. E. & Pitlick, J. Physical basis for quasi-universal relations describing bankfull hydraulic geometry of single-thread gravel bed rivers. *Earth Surface* **112**, F04005 (2007).
53. Li, G. K., Moon, S. & Higa, J. T. Residence time of over-steepened rock masses in an active mountain range. *Geophys. Res. Lett.* **49**, e2021GL097319 (2022).
54. Atwood, A. & West, A. J. Evaluation of high-resolution DEMs from satellite imagery for geomorphic applications: A case study using the SETSM algorithm. *Earth Surf. Processes Landforms* **47**, 706–722 (2022).
55. Noh, M.-J. & Howat, I. M. Automated stereo-photogrammetric DEM generation at high latitudes: Surface Extraction with TIN-based Search-space Minimization (SETSM) validation and demonstration over glaciated regions. *GIScience Remote Sens.* **52**, 198–217 (2015).
56. Jarvis, A., Reuter, H. I., Nelson, A. & Guevara, E. Hole-filled SRTM for the globe Version 4. *CGIAR-CSI SRTM 90 m Database* https://srtm.csi.cgiar.org (2008).
57. Schwanghart, W. & Scherler, D. Short communication: TopoToolbox 2 – MATLAB-based software for topographic analysis and modeling in Earth surface sciences. *Earth Surf. Dyn.* **2**, 1–7 (2014).
58. Ren, Z., Zhang, Z., Dai, F., Yin, J. & Zhang, H. Co-seismic landslide topographic analysis based on multi-temporal DEM—A case study of the Wenchuan earthquake. *SpringerPlus* **2**, 544 (2013).
59. Roback, K. The size, distribution, and mobility of landslides caused by the 2015 Mw7.8 Gorkha earthquake, Nepal. *Geomorphology* **301**, 121–138 (2018).

Acknowledgements This project was funded by NSF (1053504 and 1640894 to A.J.W.) and NSFC (42221003 and 41930864 to Z.J.). G.K.L. thanks support from a Hellman Family fellowship, a UCSB Regent's junior faculty fellowship, a USC graduate college merit fellowship and a Caltech geology option postdoctoral fellowship. We thank Z. Ren for providing the DEM data from before the impoundment of Zipingpu Reservoir, and thank M. Douglas, G. Salter, D. Okaya, V. Ganti and K. Morell for their discussions. Geospatial support for this work was provided by the Polar Geospatial Center under NSF-OPP awards 1043681, 1559691 and 2129685. This work is dedicated to a forever-remembered colleague and friend—a scientist who has been to the mountains and oceans on this planet.

Author contributions G.K.L., A.J.W., Z.J., D.E.H., A.L.D., M.P.L. and R.G.H. conceived the study. G.K.L., A.J.W., D.E.H., Z.J., F.Z., J.W. and S.D. conducted the fieldwork, including grain size measurements and reservoir surveys. H.Q., A.A. and W.W.F. contributed analytical tools and discussions. G.K.L., H.Q. and A.A. conducted analyses and calculations. G.K.L. wrote the paper with input from all co-authors.

Competing interests The authors declare no competing interests.

Additional information

Supplementary information The online version contains supplementary material available at https://doi.org/10.1038/s41586-025-09354-8.

Correspondence and requests for materials should be addressed to Gen K. Li.

Peer review information *Nature* thanks Hugh Sinclair and the other, anonymous, reviewer(s) for their contribution to the peer review of this work.

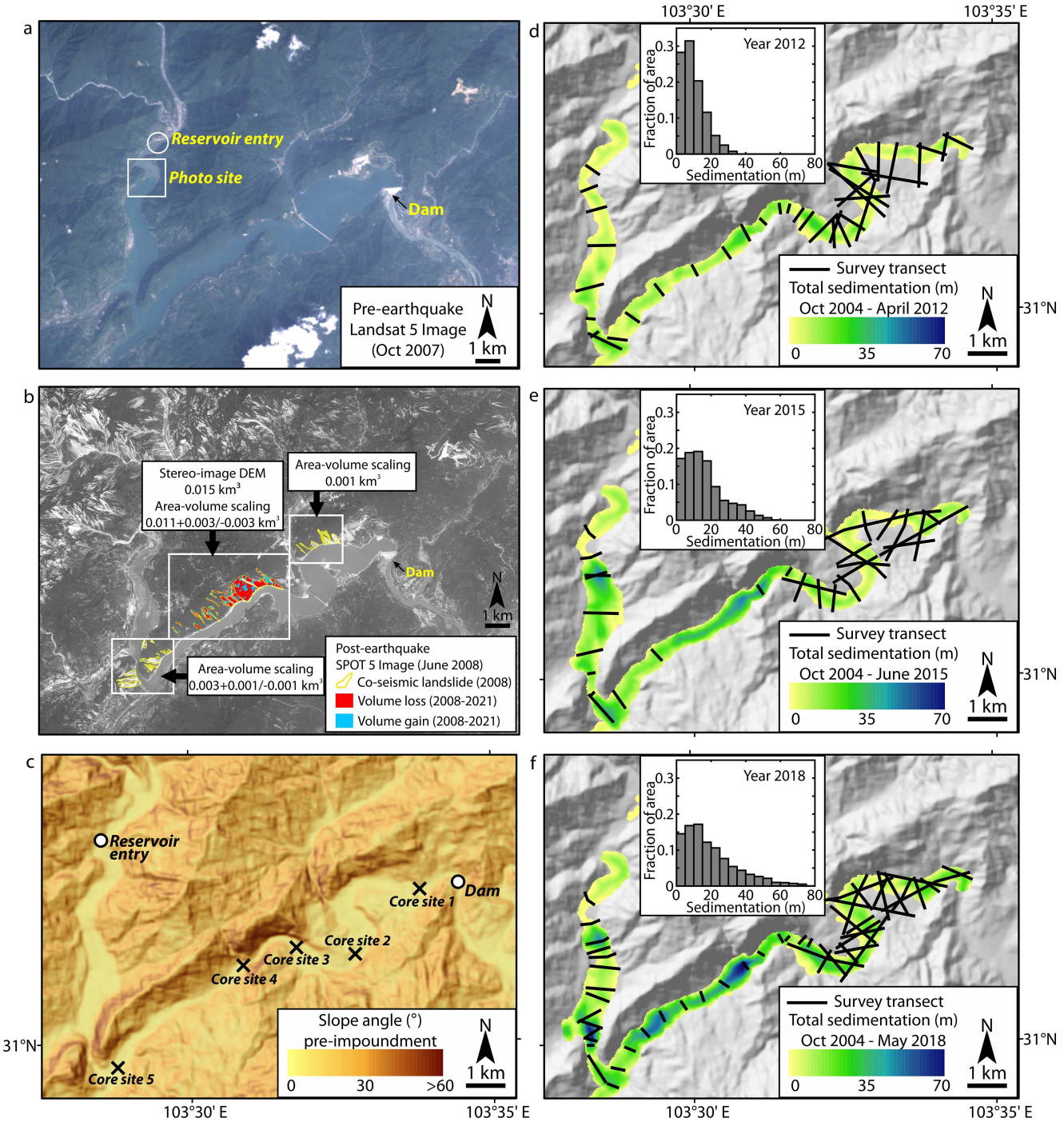

Extended Data Fig. 1 | Map view of the reservoir and pattern of sediment accumulation. Map views of Zipingpu Reservoir and sedimentation after the Wenchuan earthquake: (a) satellite image (Landsat 5) taken before the Wenchuan earthquake, showing the reservoir entry point where the Min Jiang channel widens, the site where photos in Fig. S7 were taken, and the location of the dam; (b) satellite image (SPOT 5 © 2008 CNES) of the same area taken after the Wenchuan earthquake with the mapped earthquake-triggered landslides in the reservoir area and volume changes in the landslide-affected zone determined from differencing the digital elevation models before the earthquake and in 2021 (Methods); (c) slope angles of the reservoir area with the coring sites, noting that another 10.89-m-long core was retrieved from near site 1 in 2016, as reported in prior work[24], while 1-m-long cores were taken from all sites shown here; (d-f) maps of sedimentation thickness in the reservoir in April 2012, June 2015, and May 2018, respectively, with the distributions of sedimentation thickness (bar plots) and the locations of surveyed transects (solid lines).

Extended Data Fig. 2 | Photos of coarse grains transported by the Min Jiang River and deposited in the reservoir. Map view of photo sites (a, Google Earth imagery in April 2011, Image © 2025 Maxar Technologies) and field photos (b-j) showing riverine transport of coarse grains (gravels, cobbles, boulders, indicated by arrows) entering Zipingpu Reservoir and in other tributaries of the Min Jiang basin. Note in (h), the photo shows the Yuzixi river, a tributary of the Min Jiang River, that experienced significant aggradation after the Wenchuan earthquake, with the arrow indicating a bridge that was buried during channel aggradation after the earthquake and boulders deposited on the bridge.

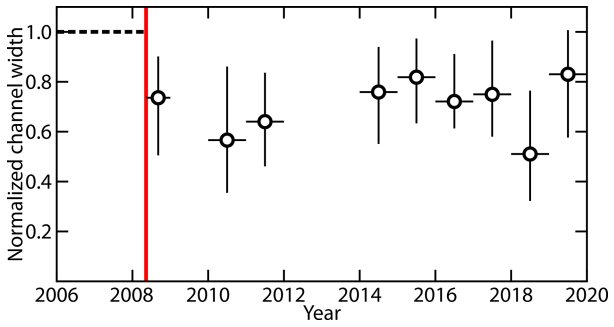

Extended Data Fig. 3 | Relative changes of width of the Min Jiang channel segment adjacent to landslides. Relative changes in channel width (normalized to averaged 2006–2008 values) after the Wenchuan earthquake from 2008 to 2019 (circles: medians of channel width normalized to the pre-earthquake channel width; vertical error bars: 16^{th}-84^{th} percentiles of the normalized channel width; horizontal bars: timespan of channel width measurement; red line: timing of Wenchuan mainshock). All data in Supplementary Table S6.

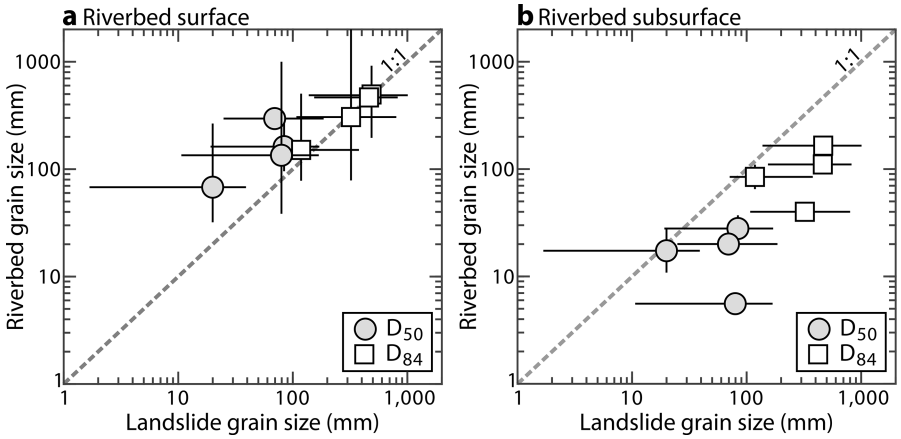

Extended Data Fig. 4 | Comparison of grain size in riverbed versus landslide sediments. Comparison between grain size (D_{50} and D_{84}) of landslide material and riverbed sediment: (a) surface riverbed sediment and (b) subsurface riverbed sediment. Each point represents data from one tributary catchment or the Min Jiang mainstem, as shown in Fig. 1 and Fig. S1. Landslide grain size data are derived from combined landslide grain size distributions upstream of each riverbed site (symbols: medians of Monte Carlo random sampling; error bars: 16^{th}-84^{th} percentiles). Riverbed sediment grain size data are estimated from combined measurements of gravel bars (symbols and error bars: means and 1σ of all grain size measurements for each site). Note that despite the differences in D_{50} and D_{84}, we observed comparable mass fraction of >0.25 mm particles in landslide and riverbed subsurface materials (Supplementary Information Fig. S6), whereas the Min Jiang suspended sediment is mostly composed of <0.25 mm particles[17]. See technical details of data collection in Supplementary Information.

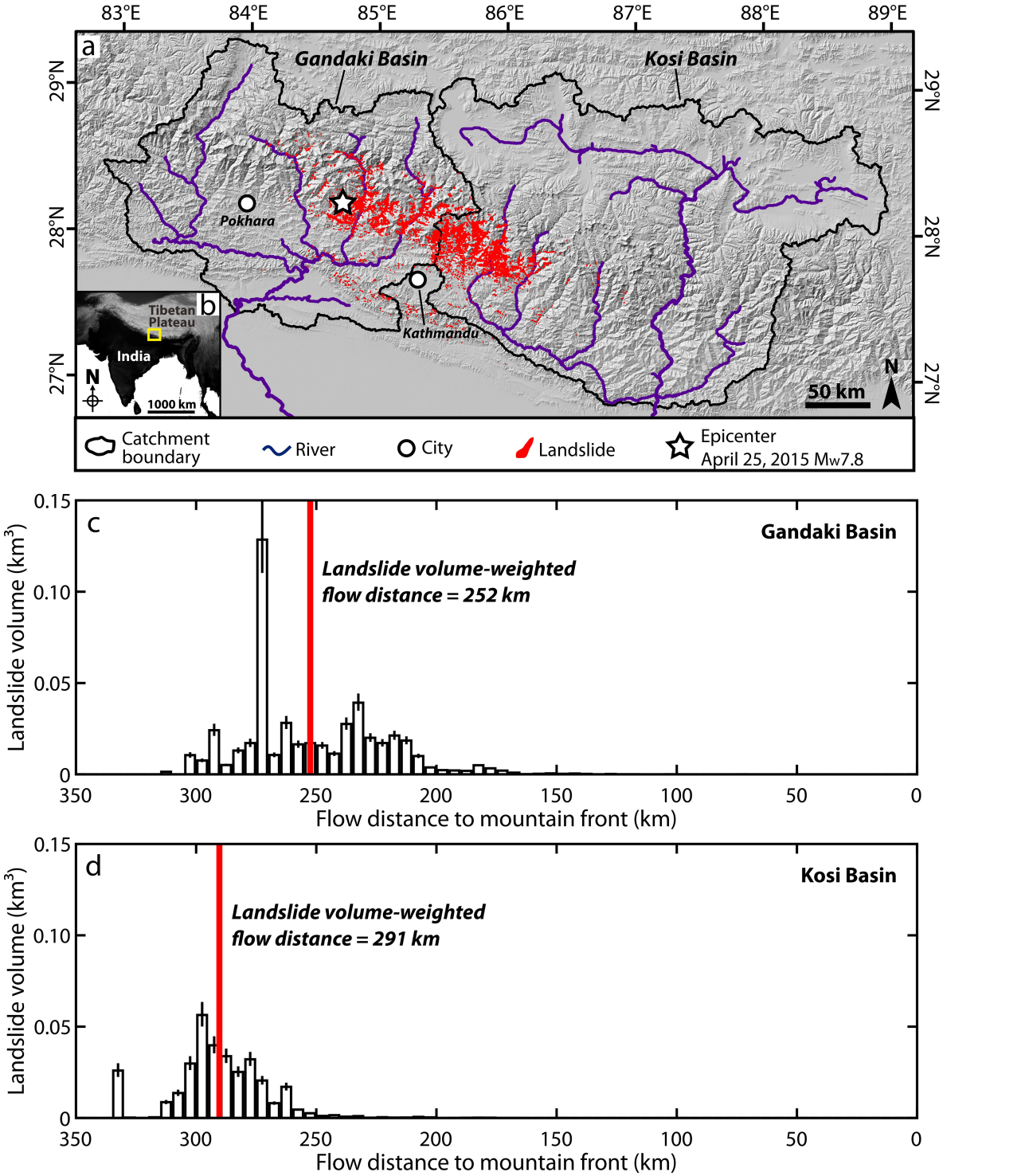

Extended Data Fig. 5 | Map view and longitudinal profile of landslides caused by the 2015 M_w7.8 Gorkha earthquake in the Nepalese Himalayas. Spatial patterns of the landslides triggered by the 2015 M_w7.8 Gorkha earthquake[59] in the context of the Gandaki and Kosi River basins draining the Nepalese Himalaya: (a) map view of the Gorkha-triggered landslides and the Gandaki and Kosi basins, (b) the regional context of the studied river basins, and (c-d) landslide volume distributions along the flow distance to the mountain front (columns: medians of landslide volumes, bars: 16th-84th percentiles from Monte Carlo simulations, red lines: landslide volume-weighted flow distance) for the Gandaki basin (c) and Kosi basin (d). Same analyses as described in the caption text for Fig. 1(e) were conducted to produce results in (c) and (d).